



ORIGINAL RESEARCH ARTICLE

# Room Temperature Mechanical Properties and Formability of $\beta$ and $\alpha + \beta$ Titanium Alloy Sheets

*Mahesh Katakam, Shailesh Maurya, Ravi Kumar Digavalli, and Suresh Neelakantan*

Submitted: 12 December 2023 / Revised: 19 May 2024 / Accepted: 24 May 2024

In the present study, the room temperature mechanical properties and formability of metastable  $\beta$ -Titanium ( $\beta$ -21S) and Ti-6Al-4V ( $\alpha + \beta$ ) alloys in sheet form are evaluated and compared. The alloys are subjected to various deformation modes, such as biaxial stretching, stretch flanging and deep drawing. Formability was characterized in terms of forming limit curve (FLC), limiting dome height (LDH), hole expansion ratio (HER) and limiting draw ratio (LDR). Uniaxial tensile tests were conducted to determine the mechanical properties, anisotropic parameters and flow curves.  $\beta$ -21S exhibited flow softening with similar strength, higher ductility and lower anisotropy than Ti-6Al-4V. Forming limit curves (FLCs) of both alloys were determined by performing tests in different strain paths using the simplified Hecker's method. The FLCs showed that limit strains of  $\beta$ -21S are marginally higher than Ti-6Al-4V. In addition, the LDH, HER and LDR values of  $\beta$ -21S are found to be higher than that of Ti-6Al-4V. Thus, the findings indicate better overall formability of metastable  $\beta$ -21S alloy making it more suitable than Ti-6Al-4V for room temperature forming applications.

**Keywords** anisotropy,  $\beta$ -21S titanium alloy, formability, mechanical properties

## 1. Introduction

Ti-6Al-4V is the most extensively used titanium alloy in aerospace and marine industries and biomedical applications such as implants and prostheses. It contains both  $\alpha$  and  $\beta$  phases at room temperature (RT), and it is the most common example of  $\alpha + \beta$  phase Ti alloys. On the other hand,  $\beta$ -Ti alloys have predominantly  $\beta$ -phase at RT, but they might also contain a small amount of  $\alpha$ -phase and other intermediate phases like martensitic phase and omega ( $\omega$ ) phase depending upon thermo-mechanical processing and heat treatment. Upon deformation, depending on the stability of the  $\beta$ -phase, they tend to exhibit stress-induced transformation, which enhances their mechanical properties (Ref 1, 2). Among the  $\beta$ -Ti alloys,  $\beta$ -21S (Ti-15Mo-2.7Nb-3Al-0.2Si) is a metastable  $\beta$ -Ti alloy that exhibits good creep resistance, high-temperature strength and superior oxidation resistance, making it suitable for military and civil aircraft. It is also used for manufacturing large and complex sheet metal parts in aircraft. For example,  $\beta$ -21S is

used for manufacturing the tail plug for the B-777 engine (Ref 3). Therefore, a study on the mechanical behavior of  $\beta$ -21S Ti alloy during sheet metal forming and its formability in different processes is important. However, the previous research (Ref 4-8) in this field has been predominantly focused on and limited to commercially pure titanium (CP-Ti) and Ti-6Al-4V alloys.

One of the earlier studies (Ref 9) on the mechanical behavior of Ti-6Al-4V alloy sheets revealed rapid necking after reaching the ultimate tensile strength, while CP-Ti demonstrated diffused necking. In another study (Ref 10) also, it was reported that the Ti-6Al-4V samples exhibited a sudden fracture without necking when deformed at RT. Djavanroodi and Derogar (Ref 12) found that the limiting strain values in the forming limit diagram (FLD) of Ti-6Al-4V increased with the increase in strain hardening exponent ( $n$ ) and normal anisotropy ( $\bar{R}$ ), thereby shifting the forming limit diagram upward. But when the Ti-6Al-4V alloy was deformed at 400 °C, the limiting major strain was found to be less than 0.1 at the plain strain condition, suggesting that the formability of Ti-6Al-4V alloy is limited even at elevated temperatures (Ref 4).

The formability of sheet metals is generally characterized in terms of stretchability, stretch flangeability and drawability (Ref 13). Limiting dome height (LDH) is a measure of the stretchability of sheets. The LDH and strain distribution in biaxial stretching are influenced by friction between the punch and the blank (Ref 14). Nitin Kotkunde et al. (Ref 4) performed the LDH test on Ti-6Al-4V at 400 °C and found that the predicted value of LDH from numerical simulation agreed with the experimental result. The hole expansion test (HET) is used to determine stretch flangeability or edge formability. The hole expansion ratio (HER) is the ratio of the final hole diameter at the time of the first edge crack to the original hole diameter (Ref 15) in a hole expansion test. The hole expansion ratio of the EDM-machined CP-Ti sample was found to be much higher than that of the abrasive water jet machined sample due to the better surface finish of the hole edge (Ref 5). Though a uniaxial

**Mahesh Katakam**, Department of Materials Science and Engineering, Indian Institute of Technology Delhi, New Delhi 110016, India; and Department of Mechanical Engineering, Rajiv Gandhi University of Knowledge Technologies Basar, Telangana 504107, India; **Shailesh Maurya** and **Ravi Kumar Digavalli**, Department of Mechanical Engineering, Indian Institute of Technology, Delhi, New Delhi 110016, India; and **Suresh Neelakantan**, Department of Materials Science and Engineering, Indian Institute of Technology Delhi, New Delhi 110016, India. Contact e-mails: dravi@mech.iitd.ac.in and sureshn@iitd.ac.in.

state of stress exists at the hole edge in HET, but conventional tensile testing methods are not suitable for finding HER. Multiple localized necking around the hole edge causes non-uniform thinning leading to higher deformation in HET, while the uniaxial tensile test results in single localized necking with uniform thinning (Ref 5). The drawability of sheet metals in the deep drawing is assessed by performing the Swift flat bottom cup test (Ref 14). Drawability is determined by the limiting draw ratio (LDR), which is defined as the ratio of the maximum blank diameter that can be successfully drawn to the punch diameter. A larger LDR value implies a larger possible cup depth, which suggests better drawability (Ref 14). In the case of CP-Ti, it was observed that the LDR increased from 2.2 at RT to 2.9 with an increase in temperature up to 200 °C (Ref 6). Thus, it indicates that the drawability increases with the increase in temperature. However, in the case of Ti-6Al-4V, an LDR of only 1.86 could be achieved at 400 °C (Ref 4).

As evident from hitherto literature, most of the work on the formability of Ti and its alloys at room temperature and elevated temperatures has been limited to CP-Ti and Ti-6Al-4V alloy sheets only. In the case of  $\beta$ -Ti alloys, researchers (Ref 11, 16) focused on the microstructural evolution and strengthening of  $\beta$ -Ti alloys through solution treatment and aging but the formability of these alloys has not been studied for applications in sheet metal forming processes. For these applications, both strength and formability are equally important. Since  $\beta$ -Ti alloys are being used for sheet metal forming applications in aircraft, it is important to characterize the formability of  $\beta$ -alloy sheets in different modes of deformation and compare it with that of a most commonly used Ti alloy such as Ti-6Al-4V to establish the specific advantages and disadvantages of these alloys in sheet metal forming. In this present work, the room temperature mechanical properties and formability of  $\beta$ -21S alloy sheets in solution-treated conditions are evaluated. This study explores formability in three different deformation modes, namely biaxial stretching, stretch flanging and deep drawing. The formability characteristics are correlated with microstructure and mechanical properties to offer comprehensive and insightful information about the material's behavior. The obtained results are systematically compared with those of commercially available Ti-6Al-4V alloy to assess the relative performance of  $\beta$ -21S alloy. This comparative analysis provides a foundation for comprehending the potential applications and practical implications of  $\beta$ -21S alloy.

## 2. Materials and Experimental Procedure

### 2.1 Materials and Conditions

The  $\beta$ -21S alloy sheets of 200 × 200 × 2 mm and the commercially available Ti-6Al-4V sheets of 500 × 500 × 1.2 mm were procured. The chemical composition of these alloys, analyzed using X-ray fluorescence (XRF), is presented

in Table 1. The as-received 2-mm-thick sheet samples of  $\beta$ -21S alloy were solutionized at 900 °C (above its  $\beta$ -transus temperature of 810 °C) for 30 min in Tempsens HTF-T-1700 furnace by applying a protective layer of delta-glaze to avoid oxidation and then water quenched to room temperature to retain the high-temperature  $\beta$ -phase. The hard outer layer of delta-glaze formed after solution treatment was removed by grinding. Most of the industrial applications, for example, compressor blades, consider the two-phase ( $\alpha + \beta$ ) microstructure of Ti-6Al-4V alloy (Ref 17). Therefore, the commercially available Ti-6Al-4V sheets, in the as-received condition, were compared with solutionized  $\beta$ -21S alloy.

### 2.2 Microscopy

The various conditions of  $\beta$ -21S and Ti-6Al-4V samples were examined using optical microscopy and X-ray diffraction (XRD) analysis. The metallographic samples were prepared as per the standard procedures of grinding, and mechanical polishing followed by etching with Kroll reagent (92% distilled water, 6% nitric acid and 2% hydrofluoric acid). Using Buehler, Ultramet 2005, the polished samples were ultrasonically cleaned in ethanol for 15 min. Optical microstructures were captured using an inverted optical microscope (Zeiss Axiovert25). Image-J (version 1.53t) software was used to estimate the volume fraction of the phases. X-ray diffraction (Rigaku Ultima IV) was used for phase identification. XRD measurements using Cu K $\alpha$  radiation ( $\lambda = 0.1542$  nm) operating at 40 kV and 40 mA were performed in the 2 $\theta$  range of 30-90° with a step size of 0.02° and scan rate of 1°/min.

### 2.3 Mechanical Properties

**2.3.1 Tensile testing.** Uniaxial tensile test was carried out using ASTM-E8 sub-size standard dog-bone samples with gauge dimensions of 6 mm width and 25 mm length to determine the tensile properties of both  $\beta$ -21S alloy and Ti-6Al-4V alloy sheets. Tensile anisotropy was evaluated using samples prepared along 0°, 45° and 90° to the RD as shown in Fig. 1. The samples were prepared using a wire EDM machine, and the tests were carried out on a 30 kN Zwick-Roell Z030 universal testing machine with a video-extensometer at a constant strain rate of 10<sup>-3</sup> s<sup>-1</sup>. The true strains in width and length directions were measured using a video-extensometer. The strength coefficient ( $K$ ) and strain hardening exponent ( $n$ ) in the power law of hardening  $\sigma = K\varepsilon^n$  were found by plotting  $\ln(\sigma)$ - $\ln(\varepsilon)$  data in the uniform plastic deformation region (i.e., between YS and UTS), where  $\sigma$  and  $\varepsilon$  are true stress and true strain, respectively.

**2.3.2 Anisotropy.** Anisotropy in terms of plastic strain ratio ( $R$ ) has been characterized as it plays an important role in processes like deep drawing. As per ASTM E517 standard, the plastic strain ratio is determined at a constant strain in the uniform plastic deformation region, but in the case of  $\beta$ -21S,

**Table 1 Chemical composition of  $\beta$ -21S and Ti-6Al-4V alloys (in wt.%)**

Alloy/element	Al	V	Si	Fe	Mo	Nb	Ti
$\beta$ -21S	3.07 ± 0.3	0.15 ± 0.03	0.40 ± 0.1	0.06 ± 0.01	13.91 ± 0.14	2.68 ± 0.02	Bal.
Ti-6Al-4V	5.74 ± 0.32	3.87 ± 0.09	0.27 ± 0.02	0.20 ± 0.01	...	...	Bal.

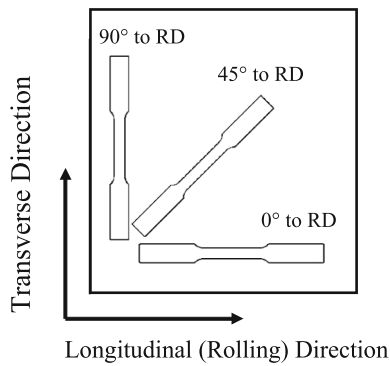


**Fig. 1** Tensile test specimen orientations with respect to the rolling direction (RD)

UTS occurs very close to YS, showing a very small uniform plastic region followed by flow softening. No standard methodology was found in the literature to determine  $R$ -values for materials showing flow-softening behavior. Thus, an alternative method of Hill's plastic strain ratio ( $R^H$ ) was adopted (Ref 18). In this method, the length and width strains were measured at different strains of regular intervals. The longitudinal and width strains were obtained continuously from the video-extensometer until fracture. The plot between these strains varies linearly, and the slope of the linear fit is used to determine the  $R^H$ -value. If  $K$  is the slope of the curve, then  $R^H$  is calculated by Eq 1 (Ref 18):

$$R^H = \frac{-K}{1 + K} \quad (\text{Eq 1})$$

Some materials show a variation of the  $R$ -value with the longitudinal strain at which it is measured. So, the  $R$ -value measured by the ASTM method is strain-dependent, while the  $R^H$ -value is strain-independent over a range of longitudinal strains even beyond uniform elongation (Ref 18). The  $R^H$  method was used to determine  $R$ -values ( $R_0$ ,  $R_{45}$  and  $R_{90}$ ) of specimens oriented at  $0^\circ$ ,  $45^\circ$  and  $90^\circ$  to RD, and the normal anisotropy ( $\bar{R}$ ) and the planar anisotropy ( $\Delta R$ ) are calculated using the following equations (Ref 13):

$$\bar{R} = \frac{R_0 + 2R_{45} + R_{90}}{4} \quad (\text{Eq 2})$$

$$\Delta R = \frac{R_0 - 2R_{45} + R_{90}}{2} \quad (\text{Eq 3})$$

## 2.4 Formability Tests

**2.4.1 Forming Limit Diagram (FLD) and Limiting Dome Height (LDH) test.** The FLDs of the two alloys were determined by following the method suggested by Hecker (Ref 19). In this method, a 100-mm-diameter cylindrical punch with a hemispherical bottom was used to deform the specimens up to necking or failure in different modes of deformation (tension-compression, plane strain and biaxial tension). To obtain the different strain paths, specimens of different widths were tested. Rectangular specimens of length 175 mm with five different widths (25, 50, 100, 125, and 175 mm) were deformed on a HIND make 100-ton formability testing machine. LDH was measured using the specimen (175 × 175 mm) which is

subjected to pure out-of-plane biaxial stretching as shown in Fig. 2(a). A blank holding force (BHF) of 500 kN was applied to prevent draw-in of the material. A circular grid with 5-mm-diameter circles with a gap of 1 mm was marked on the surface of the specimen by a 20 W fiber laser marking machine. A video camera was used to identify the initiation of the crack, and the test was stopped when a sudden drop in load at the onset of necking/fracture was observed. The major and minor strains on the deformed samples were measured in safe, necked and failed regions using a grid pattern analyzer. The major–minor strain data were used to plot the FLDs.

**2.4.2 Hole Expansion Test (HET).** Hole expansion tests were done as per ISO 16630 standards. As per this standard, square blanks of 100-mm side with a 10-mm hole at the center were used for testing. The hole in the blanks was made by a wire EDM machine. In this test, the hole was expanded with the help of a 50-mm diameter conical punch with a conical angle of  $60^\circ$  as shown in Fig. 2(b). The test was stopped when the fracture first appeared on the edge of the hole. The final thickness around the edge and the final hole diameter were measured. The ratio of the final hole diameter at fracture to the initial diameter is the hole expansion ratio (HER), and it is a measure of stretch flangeability or local edge formability.

**2.4.3 Deep Drawing Test.** A Swift flat bottom deep drawing cup test (Ref 9) was conducted for both  $\beta$ -21S and Ti-6Al-4V sheets using circular blanks of diameter ( $D_0$ ) and thickness ( $h_0$ ). Tests were carried out using a 50-mm diameter ( $D_P$ ) cylindrical punch with a 6-mm corner radius ( $R_P$ ) and 54.8-mm internal die diameter with a 6-mm corner radius ( $R_d$ ) as shown in Fig. 2(c). A blank holding force of 150 kN and 200 kN was applied to prevent wrinkling in the case of Ti-6Al-4V and  $\beta$ -21S, respectively. Lubricating oil was applied on the blank to reduce the friction between the dies and the blank. LDR was determined by increasing the blank diameter in steps of 5 mm, starting with an initial diameter of 90 mm, and testing was continued until fracture occurred. The percentage thickness variation in the deep drawn cups was measured using a pointed micrometer.

## 3. Results and Discussion

### 3.1 Microstructure

The microstructures of  $\beta$ -21S in the solution-treated condition and Ti-6Al-4V in the as-received condition are shown in Fig. 3. Due to the solution treatment at  $900^\circ\text{C}$  for 30 min, the microstructure of  $\beta$ -21S exhibits a single  $\beta$  phase, as shown in Fig. 3(a). Ti-6Al-4V has a homogeneous distribution of islands of the bcc  $\beta$  phase in the matrix of the hcp  $\alpha$  phase (Fig. 3b). The volume fraction of the  $\beta$  phase in Ti-6Al-4V was found to be approximately 28%. In contrast to Ti-6Al-4V,  $\beta$ -21S with a single  $\beta$  phase has a homogenous equiaxed microstructure. XRD peaks in Fig. 4 demonstrate the absence of the hcp  $\alpha$  phase in  $\beta$ -21S and its presence in Ti-6Al-4V.

### 3.2 Tensile Properties

The true stress–true strain curves and work hardening rate plots of  $\beta$ -21S and Ti-6Al-4V alloys obtained from uniaxial tensile tests at RT are shown in Fig. 5. The stress–strain curve of  $\beta$ -21S alloy (Fig. 5a) shows decreasing flow stress with strain for most of the plastic deformation. The negative work

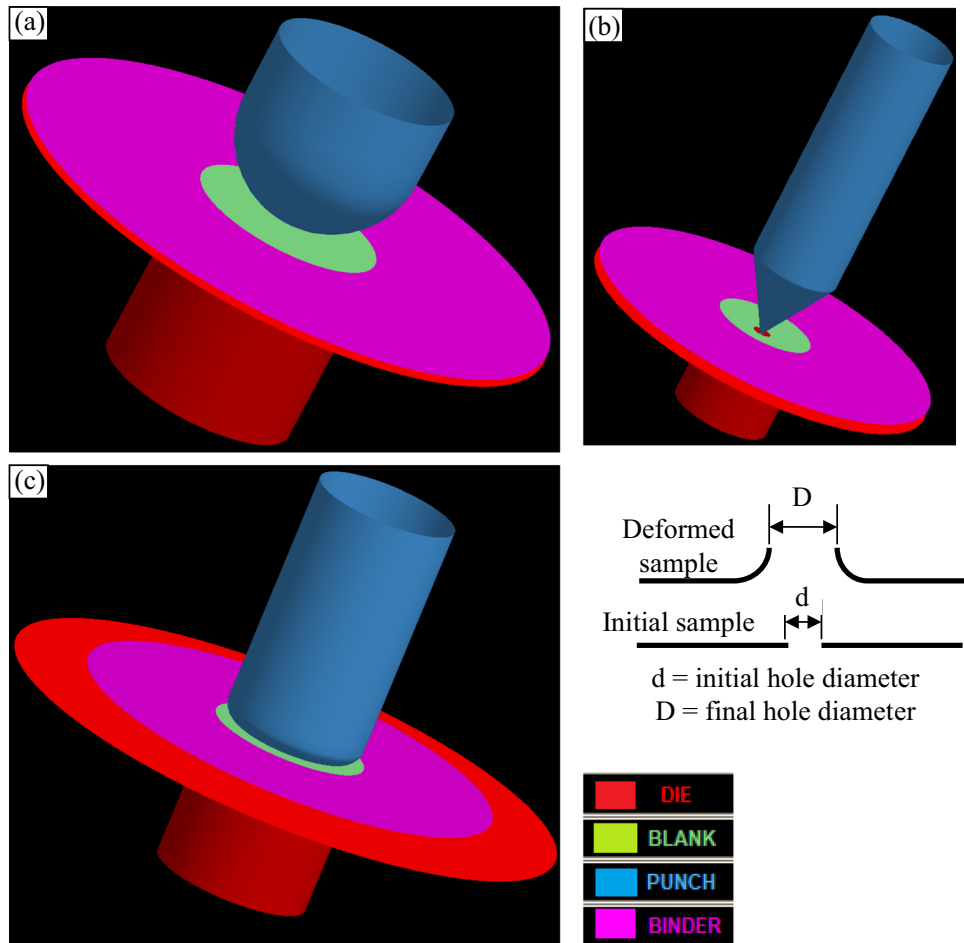


**Fig. 2** Schematic representation of (a) limiting dome height test, (b) hole expansion test (the respective diameters of the initial and deformed samples are presented below the test setup) (c) deep drawing test setup of a cylindrical cup

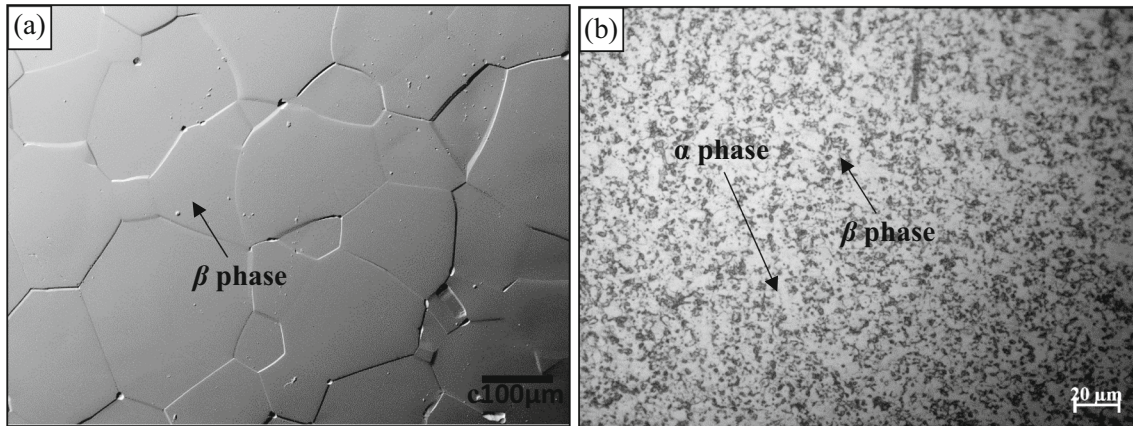


**Fig. 3** Optical microstructures of (a)  $\beta$ -21S in solution-treated condition and (b) Ti-6Al-4V in the as-received condition

hardening rate (Fig. 5c) is a clear indication of flow-softening behavior. There is no discernible difference between YS and UTS for the  $\beta$ -21S alloy since the UTS was attained relatively quickly after yielding. Similar observations of flow softening of  $\beta$ -21S alloy were reported in the literature (Ref 11, 16). However, Ti-6Al-4V alloy shows a stress-strain curve (Fig. 5b) with strain hardening behavior and positive work hardening

rate in the plastic deformation region (Fig. 5d) like many other common alloys. The possible phenomenon for such flow-softening behavior in  $\beta$ -21S alloy could be due to the intense slip band formation (Fig. 6) during deformation resulting in flow localization. The other possible phenomenon as claimed by the researchers (Ref 11, 16) was the presence of a fine athermal omega ( $\omega_{\text{ath}}$ ) phase in the alloy leading to planar

inhomogeneous flow resulting from localized near adiabatic temperature rise. The  $\omega_{\text{ath}}$  phase that forms during quenching, in the case of  $\beta$ -Ti alloys, can be easily sheared by the dislocations during plastic deformation due to its fine size, of the order of 2-5 nm (Ref 20). The subsequent dissolution of these  $\omega_{\text{ath}}$  phase particles results in easier slip activation and the formation of intense planar slip bands leading to flow localization. Hence, flow stress either decreases or remains constant after yielding. However, in the case of Ti-6Al-4V

alloy, the presence of brittle  $\alpha$  phase acts as a barrier to the dislocation movement, resulting in strain hardening.

The tensile properties of both the alloys in the three orientations to RD ( $0^\circ$ ,  $45^\circ$  and  $90^\circ$ ) are summarized in Table 2. It is observed that the Young's modulus ( $E$ ) of  $\beta$ -21S is  $\sim 38\%$  lower than that of Ti-6Al-4V. The modulus of elasticity in metastable  $\beta$  alloys is expected to vary with the presence of phases in the following order  $\omega > \alpha > \alpha' > \alpha'' > \beta$  (Ref 21). So, the presence of a single  $\beta$  phase in  $\beta$ -21S could be related to the lower modulus of elasticity when compared to Ti-6Al-4V. However, the average YS of  $\beta$ -21S was found to be  $\sim 5\%$  higher than Ti-6Al-4V, while the average UTS values of  $\beta$ -21S and Ti-6Al-4V are almost the same. The total elongation of  $\beta$ -21S was found to be 20-30% higher than that of Ti-6Al-4V. As stated earlier, the presence of brittle  $\alpha$  phase acts as a barrier to the dislocation movement and thereby improves the strength but limits the plastic deformation due to crack formation. In contrast, the single  $\beta$  phase with homogenous microstructure results in higher plastic deformation before failure. In addition, the formation of intense planar slip bands results in easier slip activation in  $\beta$ -21S (Ref 11), leading to higher ductility compared to the limited number of active slip systems in Ti-6Al-4V. Thus, diffuse necking was observed before localized necking in the case of  $\beta$ -21S, while in the case of Ti-6Al-4V, a sudden failure without diffuse necking was observed, which is consistent with the literature (Ref 13). Hence, the room temperature tensile test results show ductility

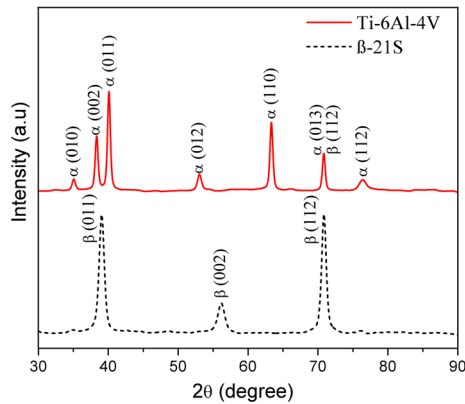


**Fig. 4** XRD peaks of  $\beta$ -21S and Ti-6Al-4V alloys

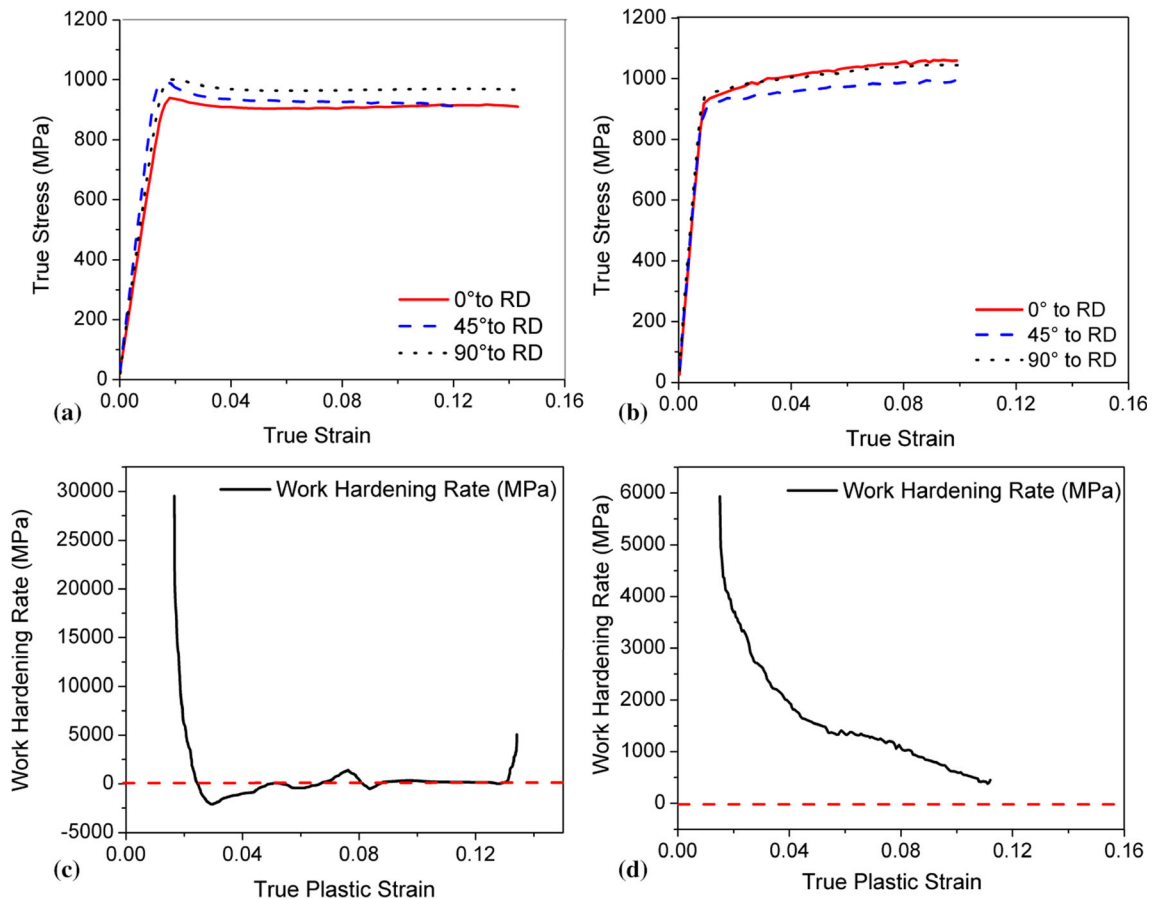


**Fig. 5** True stress–true strain curves of (a)  $\beta$ -21S and (b) Ti-6Al-4V in three different orientations to RD and the corresponding work hardening rate plots of (c)  $\beta$ -21S and (d) Ti-6Al-4V alloys along the rolling direction (RD) in the plastic deformation region

of  $\beta$ -21S is superior to Ti-6Al-4V with comparable strength values.

Since no significant hardening was observed in the flow curve of  $\beta$ -21S, the values of  $n$  and  $K$  could not be found. The  $n$  and  $K$  values of Ti-6Al-4V are given in Table 2. The  $n$  values of Ti-6Al-4V are consistent with those reported in the literature (Ref 22, 23), and the very low  $n$  values indicate the limited strain hardening ability of Ti-6Al-4V. Typically, the  $n$  value increases with increasing temperature (Ref 7, 8, 22) and decreasing strain rate (Ref 7). A high  $n$  value is preferred for better formability because it enhances the uniformity of strain distribution and hence postpones the onset of necking. This could be one of the reasons for carrying out the formability studies of Ti-6Al-4V at elevated temperatures.

### 3.3 Anisotropy

Anisotropy was observed in the tensile properties of both alloys to a limited extent. The UTS of  $\beta$ -21S along RD (i.e.,  $0^\circ$ ) is  $\sim 6\%$  lower than at  $45^\circ$  to RD. Similarly, for Ti-6Al-4V, UTS along RD is  $\sim 5.5\%$  higher than at  $45^\circ$  to RD. The plots between true longitudinal strain and true width strain are shown in Fig. 7 for both alloys. Table 3 shows  $R^H$ -values (as per Eq 1) for  $\beta$ -21S and Ti-6Al-4V along  $0^\circ$ ,  $45^\circ$ , and  $90^\circ$  to RD at a strain rate of  $10^{-3} \text{ s}^{-1}$ . It is observed that  $R^H$ -values of  $\beta$ -21S are relatively lower than those of Ti-6Al-4V, indicating lower resistance to thinning when compared to Ti-6Al-4V. Among the  $R$ -values,  $R_0$ , and  $R_{90}$  of solution-treated  $\beta$ -21S showed slightly different values from those reported in the literature (Ref 11). At a strain rate of  $10^{-3} \text{ s}^{-1}$ , the  $R$ -values of Ti-6Al-4V in this work were in the range of 0.4–0.6, while at a strain rate of  $10^{-1} \text{ s}^{-1}$ , it is in the range of 0.65–1.45 (Ref 23). To the extent

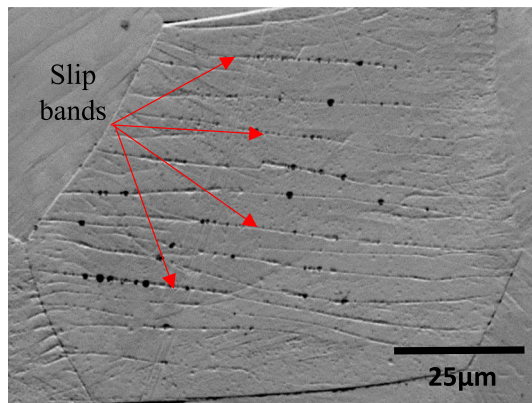


**Fig. 6** Intense planar slip bands formed during deformation in the necking region of a  $\beta$ -21S tensile specimen

of texture weakening, there would be a significant increase in the  $R$ -values, which is directly related to the formability (Ref 24). So, the variation in texture and the microstructural constituents might have played a key role in the variation of  $R$ -values.

The values of normal anisotropy ( $\bar{R}$ ) and planar anisotropy ( $\Delta R$ ) [as per equations (2) and (3), respectively] are shown in Table 3.  $\beta$ -21S shows lower  $\bar{R}$  when compared to Ti-6Al-4V. Higher  $\bar{R}$  is an advantage in processes like deep drawing and stretch flanging while a lower value of  $\Delta R$  helps in reducing the earing defect in deep drawing.  $\beta$ -21S alloy shows a significant planar anisotropy but Ti-6Al-4V show a negative value. The negative value of planar anisotropy indicates that the mechanical properties of the alloy are almost approaching the isotropic behavior. The experimental investigations of drawability and stretch flangeability would be critical to assess the formability characteristics of  $\beta$ -21S which showed flow-softening behavior with higher ductility and similar strength, but lower  $R$ -values as compared to Ti-6Al-4V.

### 3.4 Forming Limit Diagram

The experimentally determined FLDs of  $\beta$ -21S and Ti-6Al-4V are shown in Fig. 8. In the case of  $\beta$ -21S, the FLD samples showed clear necking (Fig. 9a). Hence, the limit strains at the onset of necking could be measured and they lie just above the safe strains but well below the failure strains. However, due to sudden failure in samples of Ti-6Al-4V without any visible onset of necking, the test could not be stopped at necking or the initiation of crack. So, some samples were tested up to failure (Fig. 9b), and some were stopped after reaching the maximum limit of safe region (Fig. 9c). This resulted in a large gap between the safe and the fracture strains for Ti-6Al-4V. Hence, two curves are shown for Ti-6Al-4V in Fig. 8, one representing the maximum safe strain limit and the other failure strain, while the FLD of  $\beta$ -21S represents the strains at the onset of necking.

Although void coalescence is the ductile micro-mechanism of rupture, a macroscopic mechanism of sheet rupture by fast shear was found in the case of Ti-6Al-4V at both room temperature and elevated temperatures with no evident necking (Ref 25). The absence of local necking in Ti-6Al-4V samples may also be due to negligible strain rate sensitivity coefficient ( $m$ ) and minimal fracture strain during biaxial stretching (Ref 23). Therefore, a large difference between safe and failed data points is observed on the FLD. The plain strain intercept of the curve (FLD<sub>0</sub>), which is the limiting major strain in plane strain stretching is higher for  $\beta$ -21S by  $\sim 73\%$  as compared to Ti-6Al-4V. FLD<sub>0</sub> indicates the overall level of the FLD. Also, the maximum limiting major and minor strains of  $\beta$ -21S are higher in most of the strain paths (except in some parts on the LHS of

**Table 2** Tensile properties of  $\beta$ -21S and Ti-6Al-4V alloys

	$\beta$ -21S			Ti-6Al-4V		
	$0^\circ$	$45^\circ$	$90^\circ$	$0^\circ$	$45^\circ$	$90^\circ$
Yield strength, MPa	920.0	978.8	983.0	919.6	902.4	937.8
Ultimate tensile strength, MPa	923.8	979.2	986.3	982.0	928.2	970.3
Total elongation, %	20.4	17.8	22.1	14.2	15.9	15.9
Young's modulus, GPa	58.8	75.1	63.5	105.3	105.8	110.8
Strain hardening exponent, $n$	...	...	...	0.063	0.043	0.051
Strength coefficient, $K$ , MPa	...	...	...	1234.9	1101.4	1181.1

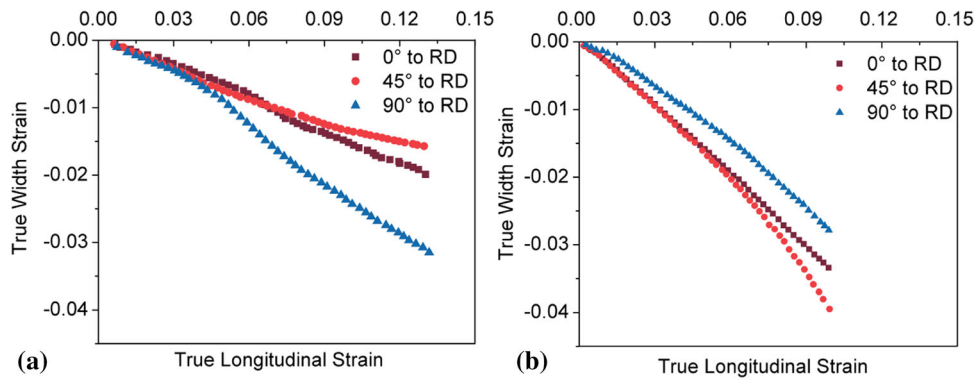


**Fig. 7** True longitudinal strain–true width strain plots used for determination of  $R^H$ -value of (a)  $\beta$ -21S and (b) Ti-6Al-4V

**Table 3** Anisotropic parameters of  $\beta$ -21S and Ti-6Al-4V alloys

	$\beta$ -21S	Ti-6Al-4V
$R^H_0$	0.19	0.52
$R^H_{45}$	0.14	0.63
$R^H_{90}$	0.36	0.40
$\bar{R}$	0.21	0.55
$\Delta R$	0.14	-0.17

the curve), which implies the overall formability of  $\beta$ -21S is better than that of Ti-6Al-4V. The higher formability of  $\beta$ -21S can be attributed to the presence of a single  $\beta$  phase with coarse grain structure and higher ductility. Interestingly, on the left side of the FLD, the room temperature safe and failure strains of Ti-6Al-4V are almost identical to the limit strains reported at high temperatures (Ref 4, 12, 23). This indicates that the room temperature drawability might result in a similar formability limit as achieved for high temperatures in the literature (Ref 4).

### 3.5 Stretchability

The LDH test samples deformed up to near necking or fracture of  $\beta$ -21S and Ti-6Al-4V alloys are shown in Fig. 10. In the case of  $\beta$ -21S alloy, the measured dome height near necking has been considered to be the LDH, while in Ti-6Al-4V, the dome height at fracture was considered. The LDH, maximum major strain, maximum minor strain and peak load values of both the alloys are summarized in Table 4. Experimental results show that the LDH of  $\beta$ -21S is 44% higher than that of Ti-6Al-4V indicating that  $\beta$ -21S is superior to Ti-6Al-4V in terms of stretchability. It is also reflected in the significant difference between the maximum major and minor strains that confirm the formability of  $\beta$ -21S in biaxial stretching is better than that of Ti-6Al-4V. The better stretchability of  $\beta$ -21S could be due to flow softening leading to larger uniform elongation prior to localized necking as indicated in the flow curve. The LDH of  $\beta$ -21S alloy at room temperature is almost equal to the LDH of Ti-6Al-4V reported at 400 °C (Ref 4). Additionally, it is demonstrated for Ti-6Al-4V that the  $n$  value increases up to 400 °C with negligible change in the  $m$  value leading to higher LDH than at 600 °C, where  $n$  is lower and  $m$  is higher (Ref 23).

The load–displacement curves of the two alloys obtained from LDH tests are illustrated in Fig. 11. The force required to reach an equal depth of deformation (say, 10 mm) is 38 to 45% lower in  $\beta$ -21S. However, due to the higher depth of forming, the peak punch load is higher for  $\beta$ -21S as compared to Ti-6Al-4V. For  $\beta$ -21S alloy, it is interesting to note that after achieving a peak load value of 120 kN, the load needed for additional deformation remains constant and is consistent with both of its samples. The higher load requirement for Ti-6Al-4V for a given depth of forming can be attributed to the pinning of dislocations during deformation due to the presence of the  $\alpha$  phase. However, in  $\beta$ -21S alloy, the ease of slip band formation initiating localized deformation might be the cause for obtaining higher deformation even at lower loads. In addition, shearing of  $\omega_{ath}$  particles by the dislocations would also contribute to the lower force requirement. As observed in Fig. 5, the stress remains constant during deformation in the plastic region before failure. Similarly, the load required for further deformation after reaching a peak value remains the same till fracture. The deformation under constant load could be related to the slip transfer that produces continuous planar slip bands, as evident from Fig. 12, favoring the deformation. The presence of planar slip bands during the plastic deformation of  $\beta$ -21S is consistent with the observations made in the literature (Ref 11). Thus, higher LDH can be produced at room temperature with lower loads for  $\beta$ -21S alloy when compared to Ti-6Al-4V alloy and thereby avoiding high-temperature complexities.

### 3.6 Stretch flangeability

A hole expansion test (HET) was performed to determine stretch flangeability. The experimentally tested HET samples of  $\beta$ -21S and Ti-6Al-4V alloys are shown in Fig. 13. The hole expansion ratio (HER), max % reduction in thickness and the peak load are summarized in Table 5 for both the alloys. In the case of  $\beta$ -21S alloy, HER was observed to be 83%, which is much higher than that of Ti-6Al-4V alloy (30.5%). Larger HER indicates higher deformation prior to edge cracks and hence thinning would be higher in the region near the crack. It is consistent with the higher maximum % thinning observed in the case of  $\beta$ -21S alloy. Punch load at failure is higher for  $\beta$ -21S due to its higher strength, thickness and extent of deformation in HET. The results indicate higher stretch flangeability of  $\beta$ -21S alloy making it more suitable than Ti-6Al-4V for applications which require high edge formability.

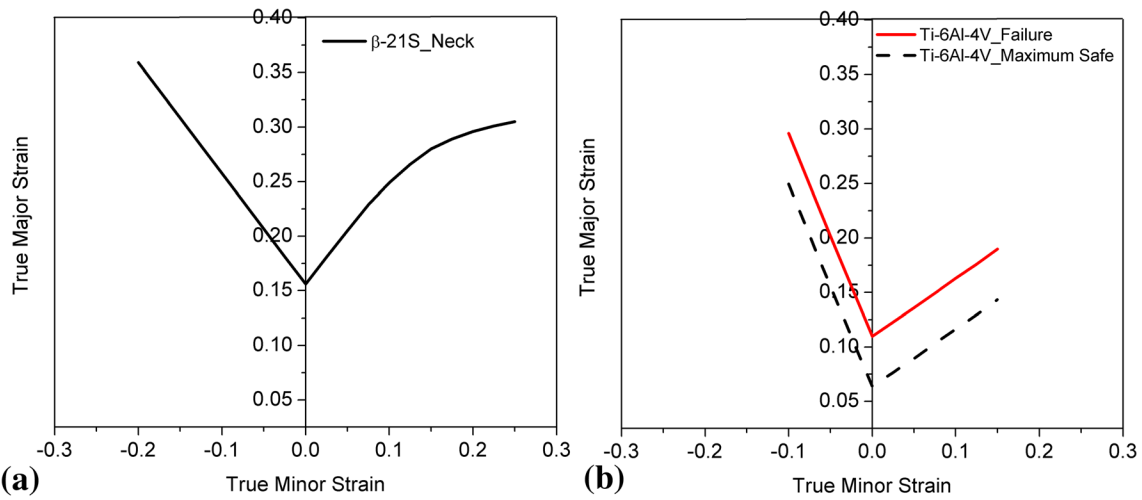


**Fig. 8** Forming limit diagrams of (a)  $\beta$ -21S (at necking) and (b) Ti-6Al-4V (maximum safe and failure)

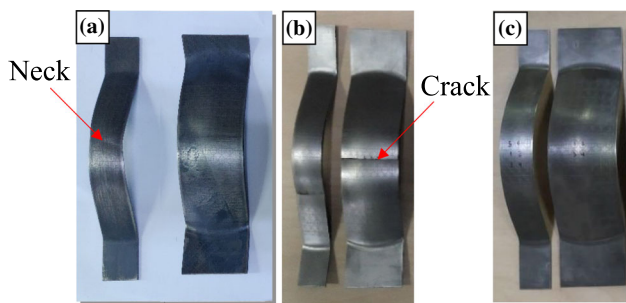


**Fig. 9** Tested FLD samples of different widths: (a)  $\beta$ -21S, (b) Ti-6Al-4V at failure, and (c) Ti-6Al-4V just before failure (maximum safe condition)

### 3.7 Drawability

Drawability was determined by finding out the LDR in the cylindrical cup deep drawing test. The experimental results of deep drawing tests are summarized in Table 6. It has been found that the LDR of  $\beta$ -21S is slightly higher than that of Ti-6Al-4V. In the case of  $\beta$ -21S, a blank with an initial diameter of 95 mm was successfully drawn, whereas a blank with a 95 mm diameter of Ti-6Al-4V failed during deep drawing. The cups, successfully drawn with a maximum diameter and the failed ones of both alloys, are shown in Fig. 14. The experimental results show an LDR of 1.8 for Ti-6Al-4V, which could be due to low normal anisotropy when compared to other ductile materials like low-carbon steel. It can also be observed that four small ears formed during the process. Slightly better drawability (in terms of LDR) was exhibited by  $\beta$ -21S in contradiction to the lower  $\bar{R}$  value when compared to Ti-6Al-4V. It could be due to the lack of a standard methodology to determine the  $R$ -value for a material showing flow softening. Thus, the higher LDR of  $\beta$ -21S alloy shall be attributed to the microstructure with single  $\beta$  phase favorable for deformation under constant stress exhibiting higher ductility. Figure 15 shows variation of percentage thinning in the experimentally deep drawn cups of  $\beta$ -21S and Ti-6Al-4V. The point “0” represents the center of the cup while the last point (9 or 13) corresponds to its flange end. It is observed that at the cup bottom, the thickness remains nearly constant, it is minimum at the punch corner radius, and it increases as we move toward the edge of the flange. This

maximum thinning in the cup wall is due to plane strain stretching, while due to circumferential compressive strains, thickening occurs in the flange area. The maximum thinning observed in  $\beta$ -21S is nearly twice that of the thinning observed in Ti-6Al-4V.

The left side of the FLD (tension-compression region in Fig. 8) of Ti-6Al-4V at room temperature (present work) and elevated temperatures (Ref 8) shows similar strains indicating that the formability in terms of its drawability would be nearly the same. This observation is well substantiated with the same LDR reported (Ref 4) at 400 °C. The negative planar anisotropy with almost similar properties in all directions is an ideal condition for deep drawing. It may be for this reason that Ti-6Al-4V exhibits LDR, which was obtained at a higher temperature, and retained at room temperature. It is also reported that the sheets with low  $\bar{R}$  value at room temperature exhibit little change or a slight drop in its value as the deformation temperature is increased, but sheets with a high  $\bar{R}$  value at room temperature retains a high value at temperatures roughly up to 800 °C. As a result, the anisotropic features of Ti-6Al-4V observed at ambient temperature are retained even at higher temperatures (Ref 26).

In summary, room temperature deformation of titanium alloys is constrained due to the limited active slip systems of the hcp crystal structure. The composition, morphology and distribution of  $\alpha$  and  $\beta$  phase decides the properties of the alloy. Interestingly,  $\beta$ -21S exhibited superior room temperature formability than commercially available Ti-6Al-4V. The coarse  $\beta$  grain structure along with the localized plastic deformation due to intense slip band formation resulted in higher ductility with comparable strength values. The ease of slip activation, slip transfer from one grain to another grain and its interaction favor higher deformations at lower loads. On the other hand, the presence of brittle  $\alpha$  phase has limited the formability of Ti-6Al-4V at room temperature.

## 4. Conclusions

The following are the main conclusions from the present study on the room temperature mechanical properties and formability characteristics of  $\beta$ -21S and Ti-6Al-4V alloys:



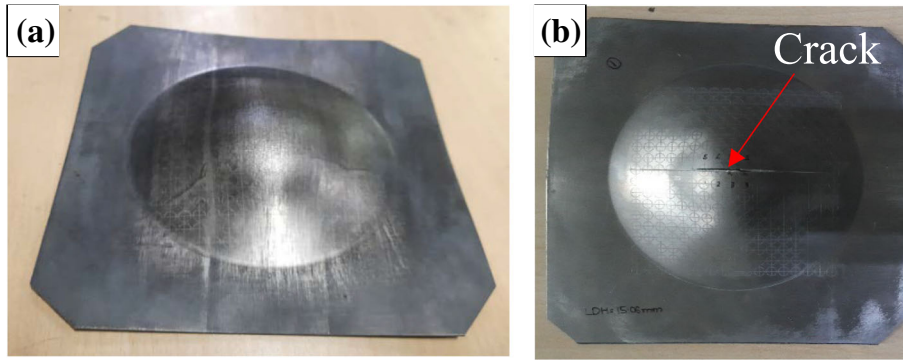


**Fig. 10** LDH test samples of (a)  $\beta$ -21S alloy and (b) Ti-6Al-4V alloy

**Table 4** Comparison of experimental results of LDH test

	$\beta$ -21S	Ti-6Al-4V
LDH, mm	21.6	14.9
Max. major strain	0.26	0.13
Max. minor strain	0.24	0.08
Peak punch load, kN	120	73

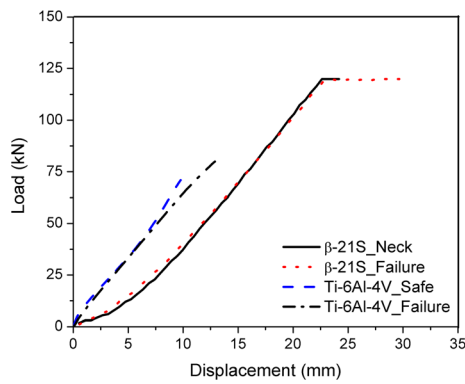


**Fig. 11** Load–displacement curves of  $\beta$ -21S and Ti-6Al-4V alloys obtained in LDH tests

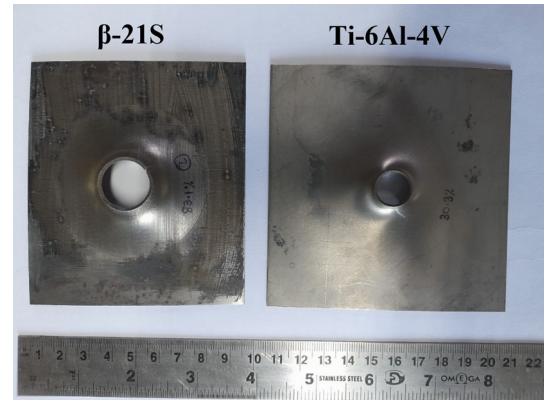


**Fig. 13** Hole expansion test samples of  $\beta$ -21S and Ti-6Al-4V alloys

**Table 5** Comparison of hole expansion test (HET) results

	$\beta$ -21S	Ti-6Al-4V
Hole expansion ratio (HER) (%)	83.1	30.5
% Reduction in thickness at the failure location	30.8	11.8
Peak punch load, kN	42	11

**Table 6** Comparison of deep drawing test results

	$\beta$ -21S	Ti-6Al-4V
Limiting draw ratio	1.9	1.8
Maximum thinning (%) (in cup wall bottom)	10.7	5.4

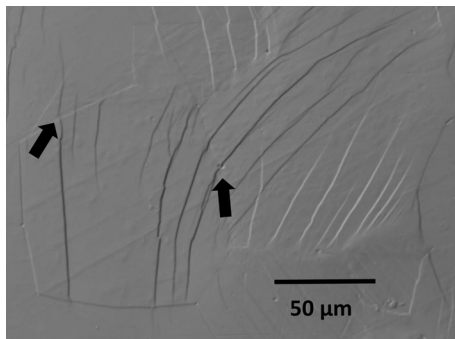


**Fig. 12** Optical micrograph showing continuous slip band formation (arrows) in  $\beta$ -21S alloy during deformation

- (1) The uniaxial tensile test of  $\beta$ -21S exhibits flow softening with a significant plastic deformation at a constant stress after the UTS resulting in higher ductility ( $\sim 20.1$  % elongation) than Ti-6Al-4V ( $\sim 15.3$  % elongation) with comparable strength values (UTS  $\sim 960$  MPa). The lower elastic modulus ( $\sim 75$  GPa) of  $\beta$ -21S suggests potential applications in areas like biomedical applications requiring high strength with low modulus.

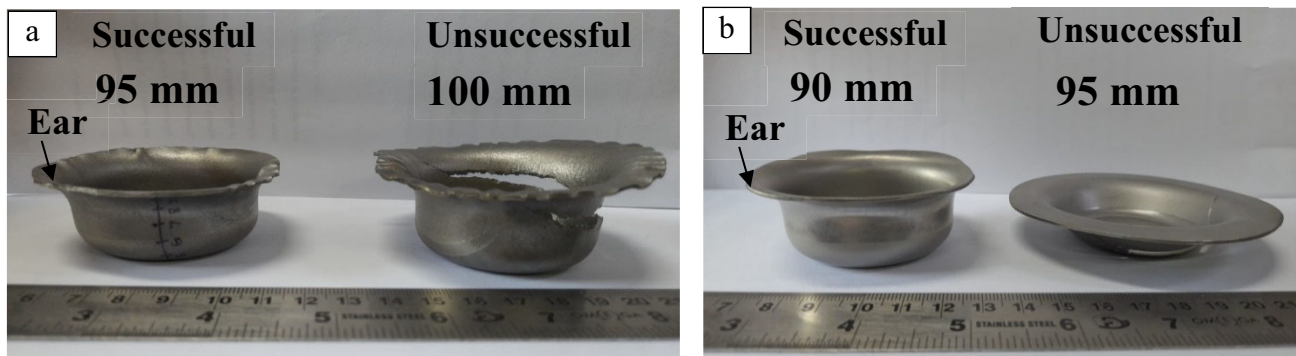


**Fig. 14** Deep drawn cups of (a)  $\beta$ -21S and (b) Ti-6Al-4V with two initial blank diameters

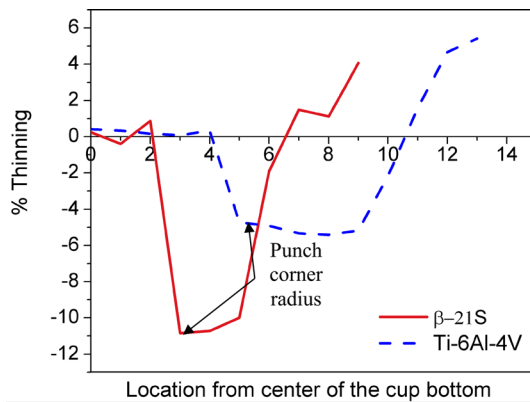


**Fig. 15** Variation of % thinning in deep drawn cups of both the alloys

- (2) The substantial plastic deformation observed in the  $\beta$ -21S alloy can be ascribed to the existence of a single  $\beta$  phase and the occurrence of flow localization caused by the development of pronounced slip bands during deformation. In contrast, the Ti-6Al-4V alloy experiences hardening due to the presence of the hard and brittle  $\alpha$  phase.
- (3) The limiting dome height (LDH) value of  $\beta$ -21S is  $\sim 44\%$  higher than that of Ti-6Al-4V, while the load required for the deformation up to a depth of 10 mm in the case of  $\beta$ -21S is  $\sim 46\%$  lower than that of Ti-6Al-4V. In the deep drawing test, the limiting draw ratio (LDR) of  $\beta$ -21S is marginally higher than that of Ti-6Al-4V.
- (4) A higher hole expansion ratio (HER) of 83.1% for  $\beta$ -21S compared to 30.5% for Ti-6Al-4V resulted in higher deformation prior to edge cracking in the hole expansion test. It clearly indicates better stretch flangeability of  $\beta$ -21S alloy.
- (5) Experimentally determined forming limit diagrams (FLDs) showed that the overall limit strains of  $\beta$ -21S are marginally higher than those of Ti-6Al-4V which is consistent with the improvement observed in three different modes of deformation. Thus, the overall formability characteristics of  $\beta$ -21S at room temperature are superior when compared to Ti-6Al-4V.

## Acknowledgments

The authors would like to acknowledge the financial support provided by Aeronautics Research and Development Board (ARDB), DRDO, India, Project No. 2017. The authors would also like to acknowledge DMRL, Hyderabad, for providing the material and the Central Research Facility, IIT Delhi for the characterization facilities.

## References

1. R. Prakash Kolli, and A. Devaraj, A Review of Metastable Beta Titanium Alloys, *Metals*, 2018, **8**(7), p 506. <https://doi.org/10.3390/met8070506>
2. J.C. Dipankar Banerjee, Williams, Perspectives on Titanium Science and Technology, *Acta Mater.*, 2013, **61**, p 844–879. <https://doi.org/10.1016/j.actamat.2012.10.043>
3. J.C. Williams and R.R. Boyer, Opportunities and Issues in the Application of Titanium Alloys for Aerospace Components, *Metals*, 2020, **10**(6), p 705. <https://doi.org/10.3390/met10060705>
4. N. Kotkunde, Amit Kumar Gupta, and Swadesh Kumar Singh, Formability study of Ti-6Al-4V alloy under warm conditions, *Adv. Mater. Process. Technol.*, 2015, **1**, p 210–222. <https://doi.org/10.1080/2374068X.2015.1118994>
5. J.S. Kwame, E. Yakushina, and P. Blackwell, Examining Failure Behaviour of Commercially Pure Titanium During Tensile Deformation and Hole Expansion Test, *J. Mater. Appl.*, 2020, **9**, p 32–37
6. F.-K. Chen, K.-H. Chiu, Formability of pure titanium sheets, 11<sup>th</sup> International Scientific Conference Achievements in Mechanical & Materials Engineering, Vol. 11, Proceedings of AMME'2002, Dec 15–18, 2002 (Gliwice, Poland) p. 39–46. [http://jamme.acmsse.h2.pl/paper\\_rs\\_amme02/1111.pdf](http://jamme.acmsse.h2.pl/paper_rs_amme02/1111.pdf)
7. A. El-Domiaty, The Effect of Strain, Strain Rate and Temperature on Formability of Ti-6Al-4V Alloy, *J. Mater. Process. Technol.*, 1992, **32**, p 243–251. [https://doi.org/10.1016/0924-0136\(92\)90181-Q](https://doi.org/10.1016/0924-0136(92)90181-Q)
8. N. Kotkunde, A.D. Deole, A.K. Gupta, S.K. Singh, and B. Aditya, Failure and Formability Studies in Warm Deep Drawing of Ti-6Al-4V Alloy, *Mater. Design*, 2014, **60**, p 540–547. <https://doi.org/10.1016/j.matdes.2014.04.040>
9. J.S. Kwame, E. Yakushina, and P. Blackwell, Examining Failure Behaviour of Commercially Pure Titanium During Tensile Deformation and Hole Expansion Test, *J. Mater. Appl.*, 2020, **9**(1), p 32–37. <https://doi.org/10.32732/jma.2020.9.1.32>
10. O.M. Badr, B. Rolfe, P. Hodgson, and M. Weiss, Forming of High Strength Titanium Sheet at Room Temperature, *Mater. Design*, 2015, **66**, p 618–626. <https://doi.org/10.1016/j.matdes.2014.03.008>
11. S.S. Satheesh Kumar, B. Pavithra, V. Singh, P. Ghosal, and T. Raghu, Tensile Anisotropy Associated Microstructural and Microtextural Evolution in a Metastable Beta Titanium Alloy, *Mater. Sci. Eng. A*, 2019, **747**, p 1–16. <https://doi.org/10.1016/j.msea.2019.01.053>

12. F. Djanvandroodi and A. Derogar, Experimental and Numerical Evaluation of Forming Limit Diagram for Ti6Al4V Titanium and Al6061-T6 Aluminum Alloys Sheets, *Mater. Des.*, 2010, **31**, p 4866–4875. <https://doi.org/10.1016/j.matdes.2010.05.030>
13. W.F. Hosford, R.M. Caddell, Metal Forming Mechanics and Metallurgy, third ed. Cambridge University Press, New York. ISBN-13 978-0-521-88121-0, 2007
14. G.E. Dieter, Mechanical Metallurgy, SI metric edition. McGraw-Hill Inc. ISBN 0-07-100406-8, 1988
15. B.M. Hance, Practical Application of the Hole Expansion test, *SAE Int. J. Engines*, 2017, **10**(2), p 247–257
16. N. Agarwal, A. Bhattacharjee, P. Ghosal, T.K. Nandy, and P.K. Sagar, Heat Treatment, Microstructure and Mechanical Properties of a Metastable  $\beta$  Titanium Alloy TIMETAL®21s, *Trans. Indian Inst. Met.*, 2008, **61**(5), p 419–425. <https://doi.org/10.1007/s12666-008-0074-6>
17. M. Soleimanzadeh and M.M. Fallah, Preform and Process Design of Ti-6Al-4V Compressor Blade Using Equipotential Lines and 3D FE Simulation, *ADMT J.*, 2018, **11**(1), p 43–50
18. Y.C. Liu and L.K. Johnson, Hill's Plastic Strain Ratio of Sheet Metals, *Metall. Trans. A*, 1985, **16A**, p 1531–1535. <https://doi.org/10.1007/BF02658687>
19. S.S. Hecker, Simple Technique for Determining Forming Limit Curves, *Sheet Metal Ind.*, 1975, **52**(11), p 671–675
20. J.A. Ballor, T. Li, F. Prima, C.J. Boehlert, and A. Devaraj, A Review of the Metastable Omega Phase in Beta Titanium Alloys: The Phase Transformation Mechanisms and its Effect on Mechanical Properties, *Int. Mater. Rev.*, 2023, **68**(1), p 26–45. <https://doi.org/10.1080/09506608.2022.2036401>
21. C.M. Lee, C.P. Ju, and J.H.C. Lin, Structure-Property Relationship of Cast Ti-Nb Alloys, *J. Oral Rehabil.*, 2002, **29**, p 314–322. <https://doi.org/10.1046/j.1365-2842.2002.00825.x>
22. S. Kumar, K. Chattopadhyay, V. Singh, Tensile behaviour of Ti-6Al-4V alloy at elevated temperatures, Proceeding of the International Conference on Multifunctional Materials, Structures and Applications [ICMMSA-2014], Dec 22-24, 2014 (MNNIT Allahabad, India), p 115–118
23. J.D. Bressan, Q. Wang, E. Simonetto, A. Ghiotti, and S. Bruschi, Formability Prediction of Ti6Al4V Titanium Alloy Sheet Deformed at Room Temperature and 600° C, *Int. J. Mater. Form.*, 2021, **14**, p 391–405. <https://doi.org/10.1007/s12289-020-01546-z>
24. R. Shabadi, S. Suwas, S. Kumar, H.J. Roven, and E.S. Dwarkadasa, Texture and Formability Studies on AA7020 Al Alloy Sheets, *Mater. Sci. Eng. A*, 2012, **558**, p 439–445. <https://doi.org/10.1016/j.msea.2012.08.024>
25. B. Valoppi, S. Bruschi, and A. Ghiotti, High-Temperature Mechanical Properties and Constitutive Modelling of Ti6Al4V Sheets, *Mater. Sci. Forum*, 2016, **879**, p 2020–2025. <https://doi.org/10.4028/www.scientific.net/MSF.879.2020>
26. P.K. Sengupta, W.T. Roberts, and D.V. Wilson, Uniaxial and Biaxial Stretching of Commercial-Purity Titanium and Ti-6Al-4V at 525°-725°C, *Metals Technol.*, 1981, **8**(1), p 171–179. <https://doi.org/10.1179/030716981803275839>

**Publisher's Note** Springer Nature remains neutral with regard to jurisdictional claims in published maps and institutional affiliations.

Springer Nature or its licensor (e.g. a society or other partner) holds exclusive rights to this article under a publishing agreement with the author(s) or other rightsholder(s); author self-archiving of the accepted manuscript version of this article is solely governed by the terms of such publishing agreement and applicable law.